ELSEVIER

Catalysis Today 64 (2001) 189–203

CATALYSIS TODAY

www.elsevier.com/locate/cattod

Measurement of hydrodynamic data of gas-phase polymerization reactors using non-intrusive methods

Apostolos Kantzas*, Ian Wright, Amit Bhargava, Fan Li, Kelly Hamilton

Department of Chemical and Petroleum Engineering, University of Calgary, Calgary, Alta., Canada T2N 1N4

Abstract

The hydrodynamic characteristics of polyethylene resins are studied in detail through a combination of different techniques in our laboratory. Computer Assisted Tomography is used to determine voidage distribution under different operating conditions. Radioactive particle tracking is used to determine the solid particle trajectories, the horizontal and vertical velocities of the solids and the residence time distribution of the solids. X-ray fluoroscopy is used to determine bubble frequency and velocity. All these techniques are then combined with the information obtained through monitoring pressure fluctuations in the fluidized bed columns. All experiments are performed in Plexiglas columns of diameters that vary between 10 and 30 cm in diameter. The materials used are polyethylene and air, respectively. The combination of these techniques provides the unique opportunity to study the fluidized bed systems in great detail. Unfortunately, all techniques cannot be implemented in a single experiment. As a result, the same experiment is repeated as many times as necessary to collect the required data. The column is moved from one imaging system to the next and the experiment is repeated under the same operating conditions. It is believed that the data collected can be used as if all the data were collected during the same test. This paper presents preliminary experimental results for each set of experiments along with the nature and limitations of each set of experimental data. The results from each different system are combined in an effort to describe the complex hydrodynamics of the bed. The incremental information obtained in each set of experiments compared to the macroscopic measurements (flow rate and pressure drop) is demonstrated.

Keywords: Gas-phase polymerization; Non-intrusive methods; Hydrodynamic characteristics

1. Introduction

The introduction of new computational fluid dynamics (CFD) models describing flow phenomena in fluidized bed reactors offers information including voidage maps, gas velocity maps, pressure distribution maps and particle velocity maps as a function of position and time and in two or three dimensions. Such models can be used for predicting hydrodynamics in the reactor. However, there is very little direct verification of all these maps, thus making the applicability of such models dubious. One way to validate such models is to perform simulations using laboratory or pilot plant scale reactors equipped with a variety of sensors that can measure reactor properties. These properties usually include local pressure and temperature measurements, superficial fluid flow rate measurements and localized measurements of bubble and solid flow through intrusive probes. Recent technological improvements in the measurement of fluid bed properties include bubble imaging using X-rays [1], tomographic imaging of voidage [2–4] and radioactive particle tracking [5–10]. These tools have the potential to provide multi-dimensional

* Corresponding author. Tel.: +1-403-220-8907; fax: +1-403-282-5060.
E-mail address: akantzas@ucalgary.ca (A. Kantzas).

0920-5861/01/$ – see front matter
PII: S0920-5861(00)00523-X

Nomenclature

A	bubble area (cm^2)
d	bubble diameter (cm)
D	bed diameter (cm)
L	bed length (cm)
u	gas velocity (cm/s)
v	solid velocity (cm/s)

Subscripts

mf	minimum fluidization
p	particle
set	solids entrained

information of properties similar to those predicted by the CFD models and the potential to verify their predictions. Even more attractive would be the possibility of using these techniques to calibrate CFD models and then applying them as tools for scale-up predictions. With these objectives in mind, the fluidization characteristics of polyethylene resins were tested in laboratory beds.

2. Experimental procedures

Investigating the combined benefits of the non-intrusive electromagnetic methods for characterizing fluid bed systems was performed using a series of simple experiments in fluidized bed models as shown in Fig. 1. The models consist of Plexiglas columns of

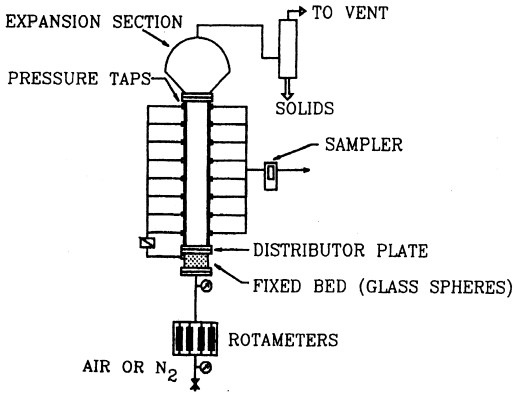

Fig. 1. Schematic of the experimental apparatus.

Table 1
Physical properties of particle systems

Code name	WPE	NPE
Mean particle size (μm)	830	543
Density (g/cm^3)	0.6585	0.6585
u_{mf} (cm/s)	12.29	12.29
u_{set} (cm/s), observed	>70	>70
Geldard classification	B	B
Sphericity	0.72	0.73

10, 20 or 30 cm in diameter and 1 m in length. The columns are filled with polyethylene resins at a settled bed of $L/D = 1$–3. The properties of the particles are given in Table 1. The samples selected for this work are a wide particle size distribution (WPE) and a narrow particle size distribution (NPE) resin from the same production batch (see Table 2). Numerous sets of experiments were performed with each particle system at the same *L*/*D*, the same distributor (porous plate), in the same column and at the same flow rates. Compressed air was used as the fluidizing medium. In order to collect the data, the column was placed in each of the measuring systems and fluidization tests were done. The inherent assumption of this approach is that duplicate runs under the same conditions will have the same fluidization characteristics. All experiments are run in atmospheric pressure and at room temperature.

2.1. Pressure fluctuation measurements

Hydrodynamic experiments were carried out by placing pressure taps on the side of the column at

Table 2
Particle size distributions for different samples

Tyler screen No.	Particle size (μm)	WPE	NPE
18	1500	0.001484	0
25	853.5	0.17417	0.004469
60	478.5	0.76263	0.973682
80	215	0.040458	0.010751
100	165	0.01229	0.005416
120	137.5	0.00345	0.002071
200	100	0.004204	0.002773
400	56.5	0.001122	0.000777
635	29	0.000191	6.07E−5
Pan	20	0	0

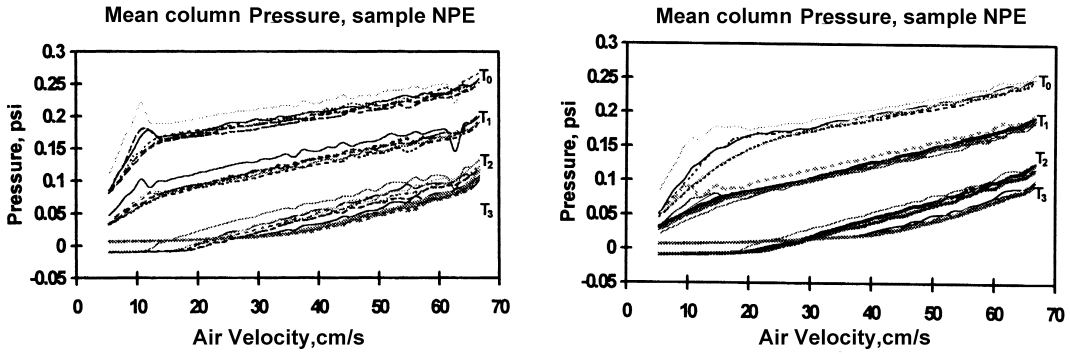

Fig. 2. Typical pressure transducer response, minimum fluidization experiment.

various heights and by logging the pressure data for a wide range of airflows and for both types of solids. The pressure taps were placed at the level of the distributor plate and then at intervals, approximately 17 cm, up the column. These taps were connected to transducers at the bottom of the column with $\frac{1}{8}$ in. (0.32 cm) nylon tubing.

The pressure transducers used to collect the pressure tap data are Schlumberger Solartron transducers, model 8000DPD. Four such transducers were used, three with full scale 0–199 kPa and one with 0–27.4 kPa. These transducers produced a 4–20 mA signal, which was run through a resistor of approximately 250 Ω giving a signal of 0–5 V. An ADC converter read the voltage through the conversion resistors on a PC-LPM-16 card from National Instruments, which was mounted in an ALR-386 personal computer with 16 MB RAM. Calibration curves for the pressure–voltage relationship were prepared and used to convert the logged voltages to pressures. Details of the experimental apparatus and the results obtained are documented elsewhere [12].

The hydrodynamic experiments were carried out in a series of steps. First, the column was charged with the solid material and was fluidized sufficiently to eliminate possible packing effects. The airflow was then stopped. Measurements were taken by setting the airflow according to a rotameter using a pressure regulator. When the airflow reached a fixed rate, the voltages from the transducers were sampled at a frequency of 100 Hz for approximately 20 s. The airflow was then adjusted to a new value and the measurement was repeated. These steps were carried out by starting at the lowest airflow measurable by the rotameter, then by increasing flow by 2% of its maximum range until the highest airflow was attained. The process was then repeated at decreasing gas flow rates. A total of three sets of increasing and decreasing airflow data were acquired.

The voltage data from the transducers was transferred to an IBM RS6000 workstation where analysis was carried out using Matlab-4.5®. The voltage data was converted to pressure data using the prepared calibration curves.

The design of Fig. 1 is subjected to a significant amount of backpressure. This was reflected in the data collection (see Fig. 2). A separate experiment was carried out keeping all the operating variables the same as in the hydrodynamics experiments but with the column empty. The mean pressures for each sample of this data was used to fit a fourth order polynomial for the backpressure to approximately 1% accuracy. This polynomial was then subtracted out of the pressure data for the hydrodynamics experiments thus leaving the column pressures free of artifacts.

2.2. X-ray Computer Assisted Tomography

Computer Assisted Tomography (CAT or CT) is a tomographic imaging technique that generates cross-sectional images in the axial plane. The images produced are maps of the relative linear attenuation values of objects. For a fixed position of the X-ray tube, a fan beam is passed through the object and measurements of transmitted X-ray beam intensities are made by an array of detectors. Measured X-ray

transmission values are called projections. CT images are derived by mathematical analysis of multiple projections. The relative attenuation coefficient is normally expressed in Hounsfield units (HU) which are also known as CT numbers. A detailed description of the capabilities of CAT scanning is presented elsewhere [2–4]. Specifications of the scanners used are spatial resolution 0.4 mm × 0.4 mm in plane by 3 mm thickness and temporal resolution 3 or 2 s depending on the mode used. The source is a rotating tube with over 900 fixed detectors (fourth generation), operating on a fan beam geometry and standard back-projection reconstruction.

2.3. X-ray imaging

An image intensifier (II) is used to convert incident radiation into a light image to be viewed, recorded or photographed. An II consists of an evacuated glass, aluminum or non-ferromagnetic envelope that contains an input phosphor, photo-cathode, electrostatic focusing lenses, accelerating anodes and output phosphor. The input phosphor absorbs X-ray photons and re-emits part of this absorbed energy as a large number of light photons. Light photons emitted by the II input phosphor are absorbed by a photo-cathode, which emits photoelectrons. The photoelectrons are accelerated across the II tube by the anode and focused on the output phosphor by an electrostatic lens. These electrons which have energies of 25–35 keV, are absorbed by the output phosphor and emit a large number of light photons. Thus, the pattern of incident X-ray intensities at the input phosphor is converted into an intense pattern of light at the output phosphor of the II. X-ray fluoroscopy experiments are run using a GE MPX-100 system [11]. Two-dimensional images of the fluidized bed experiments are obtained in real time. Currently, these experiments are video-recorded. Selected images are digitized and are used for analysis of the bubble shapes and sizes. Although the X-ray system has a pulse of 1000 Hz for image acquisition, the controlling step for sequential images is the frequency of recording, which was 30 frames/s in this work.

2.4. Radioactive particle tracking

Radioactive particle tracking experiments were performed using a gamma-camera system. There are a number of different types of gamma cameras available on the market but the principle of operation remains the same for all. The models available in our laboratory are a Siemens Orbiter and a Siemens ZLC, which have 75 photo-multiplier tubes (PMT) and a NaI crystal diameter of 41 cm. Details on the operation and specifications of the gamma cameras are given elsewhere [8–10].

Tagging a given particle of polyethylene with Technetium macroaggregated albumin (99 mTc-MAA) allowed performing particle-tracking experiments for the polyethylene resins. The choice of radio-pharmaceuticals as opposed to other approaches in the literature was taken so that short half-life material could be used for the tests thus eliminating the need for sophisticated disposal methods. Furthermore, the use of commercially available imaging systems eliminates the need for custom-made software and hardware development.

Each experiment is performed with the placement of the column that includes the radioactive particle in front of the camera. The camera acquires images of the field of view and stores them in arrays of specified sizes. The arrays used in this paper are 128 × 128 elements. The resulting pixel size of 3.2 mm is the level of uncertainty for the location of the particle. Updated images with the location of the particle are obtained with a frequency of 20–50 Hz. The choice of frequency depends on the activity and the velocity of the radioactive particle.

3. Results and discussion

3.1. Pressure fluctuation measurements

When analysis of the pressure tap data was carried out, three different measures of the pressure data were considered. First, the mean pressure vs. air velocity was calculated and plotted. This is the traditional way of looking at the pressure in a fluidized bed. Second, the relationship between the air velocity and the standard deviation of the pressure signal was examined. This should give an indication of relative bubble size. Finally, the frequency of the fluctuation in the signal was also examined to quantify bubble and slugging frequency.

Analysis of the mean pressure was straightforward. The mean of each pressure sample was calculated and plotted against the air velocity at which that sample was taken. In all cases, this was done for all four-pressure transducers on the same plot. Fig. 2 shows a set of typical results. The curve for pressure transducer T_0 located at the distributor plate is equivalent to the traditional pressure vs. fluid velocity plot used to determine the minimum fluidization velocity. The curve for T_1 is similar to the curve for T_0 suggesting that placement of the transducer at an intermediate height up the column is equivalent to placement of the transducer at the distributor of a shorter column. Interestingly, the minimum fluidization numbers from the T_1 curve are essentially identical to the minimum fluidization numbers from the T_0 curve demonstrating that minimum fluidization is not occurring at different heights in the bed at different velocities. The other features of interest in the T_0 and T_1 curves is that they are linear below minimum fluidization, passing though (0, 0), with a very small difference in the rising and falling curves for the two different particle size distributions of polyethylene. In the polymer cases, there is a much greater difference in this part of the plots with the decreasing curves showing a curved region around minimum fluidization. Above minimum fluidization, the most remarkable feature of all the plots is that they show a definite increase in the pressure drop across the bed as the velocity is increased. While this is to be expected in fixed beds, in fluidized beds the traditional experience is that the pressure is constant with increases in fluid flow until the fluid flow is fast enough to cause significant entrainment. In all cases the T_2 and T_3 pressure curves remain flat until the bed has expanded sufficiently to cover the taps. They are similar to those from lower in the column except for the expected shift in the pressure drop. For all of these curves, the T_3 curve is above the T_2 curve for lower air velocities. Further investigation revealed that the T_2 tap was partially plugged.

The purpose in examining the standard deviation of the pressure measurements was to gain some insight into the hydrodynamic regimes under which the column is operating [13,14]. Since the polymer particles are both unusually large and light there is some question as to whether the currently available correlations can accurately predict the hydrodynamic regime. There is a pressure field associated with each bubble in the column, thus the passage of bubbles can be detected as a fluctuation in the pressure, with larger bubbles giving larger fluctuations. The magnitude of the fluctuations can be measured as the standard deviation of the pressure samples. Since slugs are the largest bubbles possible in the column, the slugging regime should be detectable as a peak in the standard deviation of pressure vs. fluid velocity curve.

The bubbling regime is identified to the lower side of the velocity curve and the turbulent regime to the higher side of the velocity curve. None of the curves obtained in this paper have such a peak. These curves are flat from zero flow to minimum fluidization where they make a small sudden jump. Fig. 3 shows a typical example. The polymer plots show a region of nearly constant fluctuation magnitude before curving into a linear increase in fluctuation magnitude with increase in fluid velocity. The fact that these plots do not show

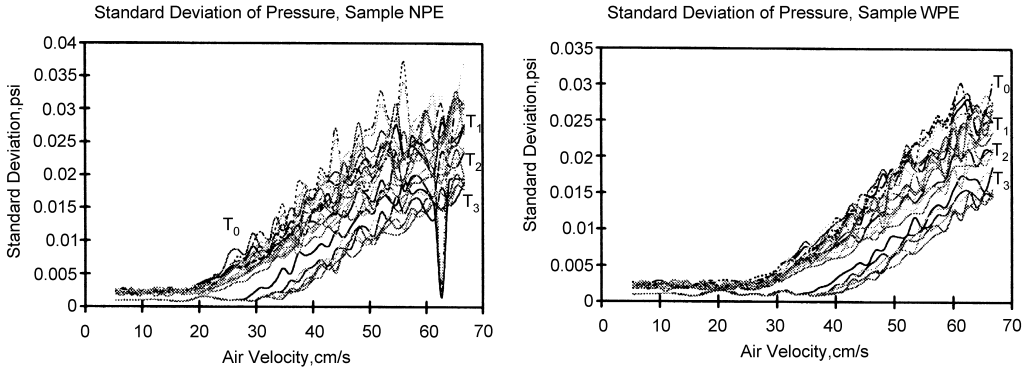

Fig. 3. Standard deviation of pressure signal as a function of air velocity for polyethylene data.

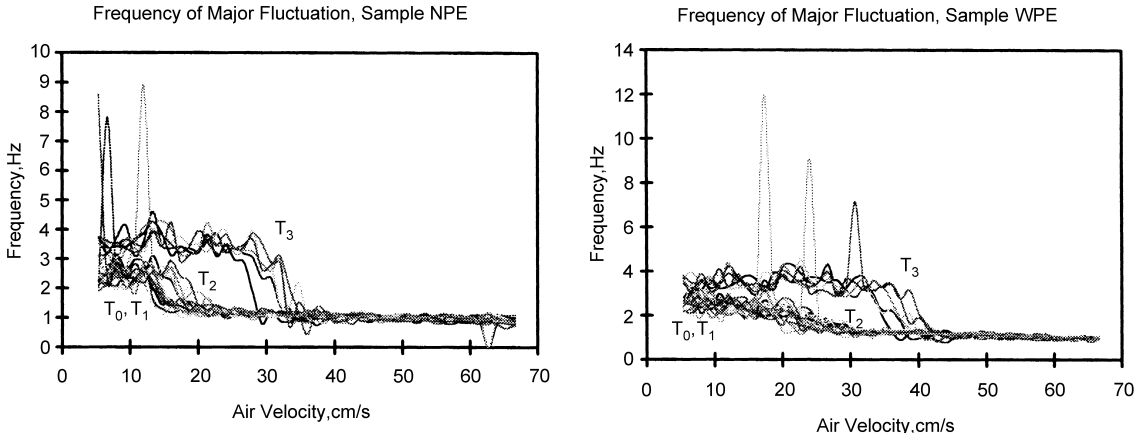

Fig. 4. Fluctuation frequency for polyethylene data.

the expected peak is a reflection of the fact that the fluid flow had not increased beyond a point where significant carry-over would result from slugs of material being pushed to the top of the column and then blown out. If the column was considerably taller, it may have been possible to run at a sufficiently high velocity to see this peak. However, the geometry and loads in the laboratory column are similar to that of plant reactors. It is believed that for this specific case much taller columns of the same diameter would not give data that can be translated to actual reactor conditions.

In any case, in our experiments it was observed that the region of low fluctuation magnitude between minimum fluidization and the transfer to the linear rising section indicates a regime of a few small bubbles and little if any particulate circulation in the column. The lower part of the increasing region indicates vigorous fluidization with large-scale circulation of particles in the column. The upper part shows slugging which is nothing more than the condition where, under vigorous fluidization, the bubbles have increased in size to the same order as the column diameter.

The frequency of major fluctuation [15,16] in the pressure measurement may be reasonably assumed to increase with increasing air velocity. More air passing through the column implies more bubbles to move through. This is not the case. All the plots show high fluctuation frequency for velocities below minimum fluidization. This is an artifact caused by signal noise. When the fluctuation caused by the bubbling bed becomes noticeable, the noise no longer affects these plots. The NPE cases show an immediate drop in fluctuation frequency at minimum fluidization.

The WPE cases show a gradual drop in fluctuation frequency from the minimum fluidization velocity to the velocity marking the transfer from low bubbling to vigorous bubbling as determined by the standard deviation of the pressures. At velocities above this transfer region, in all cases, the fluctuation frequency follows a linear relation to velocity with a small decrease in fluctuation frequency with velocity. This indicates that there is a significant difference in the nature of the bubbles between these two regimes with many small bubbles in low bubbling conditions and fewer large bubbles in vigorous bubbling conditions. A typical example is shown in Fig. 4. There is no apparent variation from vigorous bubbling to slugging.

3.2. X-ray imaging

For each set of experiments several minutes of video recording were performed for the 10 cm diameter fluidized bed column. There were two to three sets of recordings made (one at the top part of the column, one at the middle part of the column, whenever possible, and one at the bottom part of the column) for each set flow rate. The video recording provided two-dimensional images with frame frequency of 30 Hz. Bubble frequency and velocity measurements were performed through the inspection of the individual frames. Data on bubble size and geometry were

obtained through the imaging of individual frames and the utilization of imaging software.

The bubble tracking and marking computer programs mark bubbles from the top to the bottom of the frame. The marking strategy is to marking bubbles from top to bottom and from left to right of the frame. Bubbles in the first frame are identified as bubble 1 bubble 2 and so on. If other bubbles come on next frame sequential numbers are given to them. The total number of pixels multiplied by pixel size is counted as the original bubble size cross-sectional area. Assuming that bubbles are spherical and their silhouettes are circular, then the bubble diameter (d) can be calculated by the following simple equation:

$$d = \sqrt{\frac{4A}{\pi}}$$

The tracking programs can automatically record the coordinates (x, y) of the bubble center for every frame tracked. The center of a bubble is defined as the geometric center of the original bubble area. For example, the programs record the center coordinate of bubble 1 on the first frame. When the programs track the second frame and if bubble 1 still on the second frame, the center coordinate of bubble 1 is also recorded so that the distance that bubble 1 travels in both vertical and horizontal directions can be calculated. The vertical and horizontal velocities of bubble 1 can then be easily calculated by dividing the travel distances with the time step between two successive frames, which is $\frac{1}{30}$ s in this study. The velocity calculation is illustrated in Fig. 5. Details are shown elsewhere [11].

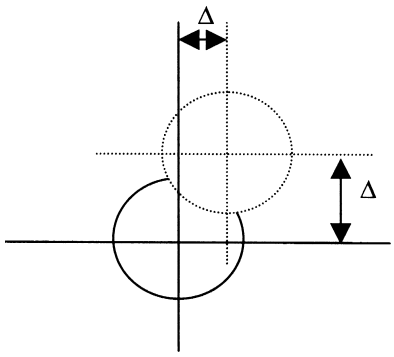

Fig. 5. Simplified schematic for bubble velocity calculations.

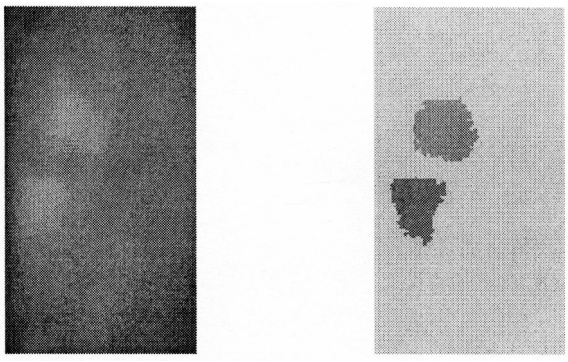

Fig. 6. Sample X-ray image for bubbling polyethylene column near the distributor.

Fig. 6 provides a typical example of images obtained from the recorded videotape. During the imaging stage of the experiment, very high quality pictures were obtained in the X-ray II screen. Bubbles were observed to coalesce into larger bubbles as gas moves towards the top of the bed (as expected). Slow and vigorous bubbling as well as slugging was clearly observed.

With respect to sample WPE, the following observations were made. At fluidization number 1.1, bubbling was not always visible. This was partially attributed to the instability of the incoming air stream. However, when bubbles were observed, they tended to be in a small channel along a narrow path of the column. Small jet-like structures were observed with the bed being locally entrained at that time, although the distributor is a porous plate. However, these structures were unstable and were at the initiation stage of bubbling. Such onset of bubbling was not observed with any other tools thus giving an advantage to the use of the X-ray imaging apparatus. There was no uniformity in the bubbles produced. Bubbles appeared to be uniformly spreading across the bed cross-section at a height that was approximately 1.7D. At this location bubble sizes appeared to be up to 3 cm in diameter. At fluidization number 2.2, the column was vigorously bubbling. At the distributor plate, bubbles formed at the center rather than at the sides of the column. Bubble coalescence created bubbles of sizes up to 5 cm at a height of 0.9D. Moving towards the middle of the column, the bubbles further coalesced to form larger bubbles or slugs at a height of 2.5D. At the top

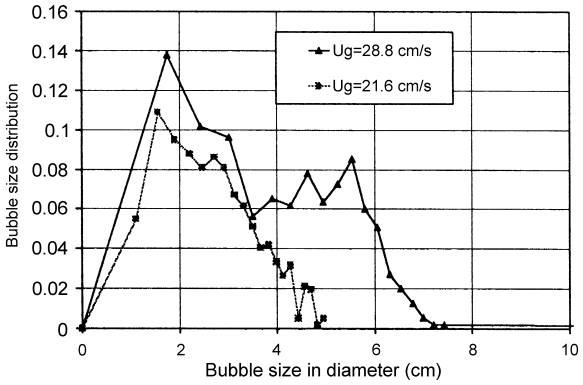

Fig. 7. Bubble frequency estimations for narrow particle size polyethylene resins as obtained from inspection of X-ray imaging data.

of the column, the bubble diameters ranged from 3 to 10 cm. At fluidization number of 2.75, bubbles at the distributor appeared at the sides of the plate. Bubble coalescence was evident at 0.9*D* at which point bubble sizes were up to 5 cm. At 1.7*D* some slugging appeared. At this point, most of the bubbles seemed to spread across the bed diameter and the sizes increased from 3 to 10 cm. Several slugs appeared that traveled and burst at the top of the column. Towards the top, small bubbles rarely appeared. Most of the bubbles were larger than 5 cm in diameter. Large elongated bubbles also appeared frequently.

Sample NPE seemed to behave similarly to sample WPE as indicated in the video images and the reported minimum fluidization velocity. This observation contradicts previous observations with other polyethylene resins [2,3] and is the object of further investigation.

Figs. 7 and 8 present bubble size and bubble velocity frequency distributions for tests in the NPE sample.

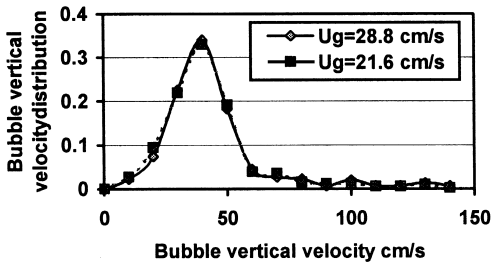

Fig. 8. Bubble velocity estimations for narrow particle size polyethylene resins as obtained from inspection of X-ray imaging data.

Two different gas velocities are presented. The bubble size frequency extends significantly with velocity, while the corresponding bubble velocities seem to be unaffected by the increasing gas velocity.

3.3. Radioactive particle tracking

For each set of experiments, several thousands of images containing the radioactive particle were collected. Sample WPE was run over a period of 3 h resulting in 36 000 images being collected at three different gas velocities (11.26, 16.52, 21.77 cm/s, respectively). The approach was to collect data at the lower rate, increase the rate to the next value, collect a series of images, increase the rate, collect data, reduce the rate to the initial value and start again. Thirty-six sets of images were acquired. Analysis of the sequential images provided the position of the radioactive particle (*X*- and *Z*-dimension), and the particle velocity (*X*- and *Z*-direction). Information in the *Y*-direction is not considered in this study because it was found that the particle activity variability with depth had low resolution. This issue was addressed through the acquisition of a second camera to collect data in a perpendicular direction [17,18]. Further analysis of the gamma camera images provides frequency distributions of the particle positions and velocities that can be fitted into analytical functions. In a second set of experiments with the same resin, twenty-eight 1000 frame sets at five different velocities (13.51, 20.27, 27.03, 33.78 and 40.54 cm/s, respectively) were analyzed in the same manner as described above. Finally, in a third set of experiments, 36 000 images were collected with sample NPE and at velocities of 13.51, 20.27 and 27.03 cm/s, respectively, were further analyzed in the same manner. Some typical examples are included. The tracer particles used for samples WPE and NPE had dimensions of 800 and 600 μm, respectively. The corresponding gas velocities to rotameter settings are shown in Table 3.

Fig. 9 shows the residence time distribution images for selected rates. The three selected images are presented in order to demonstrate good mixing, poor mixing and trapping of the particle in stagnant zones. It was observed that at low rates, invariably the particle spent most of the flight time oscillating within a very small area. It was also found that the particle would not reach the bottom part of the column. As also

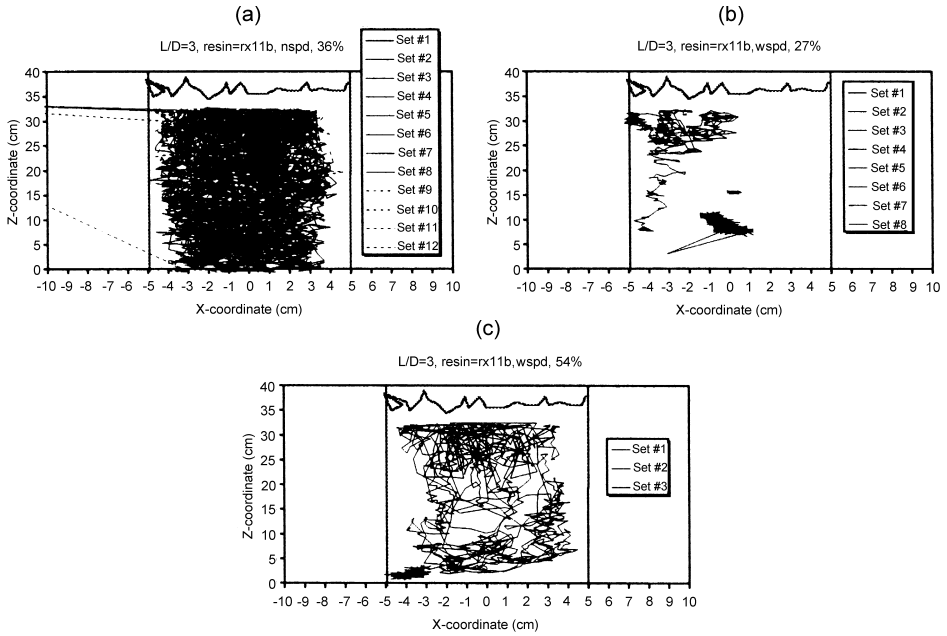

Fig. 9. Residence time distribution images for samples WPE and NPE: (a) good mixing, (b) poor mixing, (c) trapping of the particle in stagnant zones.

evident from the images presented, when the particle reached the bottom of the column, it would remain trapped (with the notable exception of the first image of Fig. 9 where good mixing is achieved). Generally speaking, it was found that the particles also stayed away from the walls of the bed. The existence of stagnant zones was also verified by visual inspection of the X-ray images.

Although the images of Fig. 9 show a decent picture of the quality of particle mixing in the bed, they are difficult to read. Thus, examples of the corresponding *X*- and *Z*-position variability are presented here as well. Fig. 10 depicts the *X*-position variability for the data presented in Fig. 9. When good mixing occurs, it is accompanied by wide fluctuations of the particle in the *X*-direction. The opposite is observed when the fluctuations are small.

In Fig. 11, the *Z*-position variability for the data of Fig. 9 is presented. When comparing Figs. 10 and 11, we can clearly observe that the variability of *Z*-position is correlated to the variability of *X*-position. From all the samples analyzed to date, this type of behavior is normal.

In Fig. 12, the frequency distributions for all *X*-positions for WPE and NPE sets of experiments are presented. It can be seen that there is an insignificant association between the particles and the wall. This implies that stationary or near stationary particles cover the wall surface. This observation is consistent with previously reported data [2,3] and it can be attributed to static forces in the bed. In many cases, the frequency data were fitted well by a quadratic function. This is a topic of further investigation.

In Fig. 13, the frequency distributions for the *X*-velocities for both WPE and NPE sets of experiments

Table 3
Gas velocity vs. rotameter settings for Figs. 9–15

Rot. (%)	*u* (cm/s)
15	11.26
18	13.51
22	16.52
27	20.27
29	21.27
36	27.03
45	33.78
54	40.54

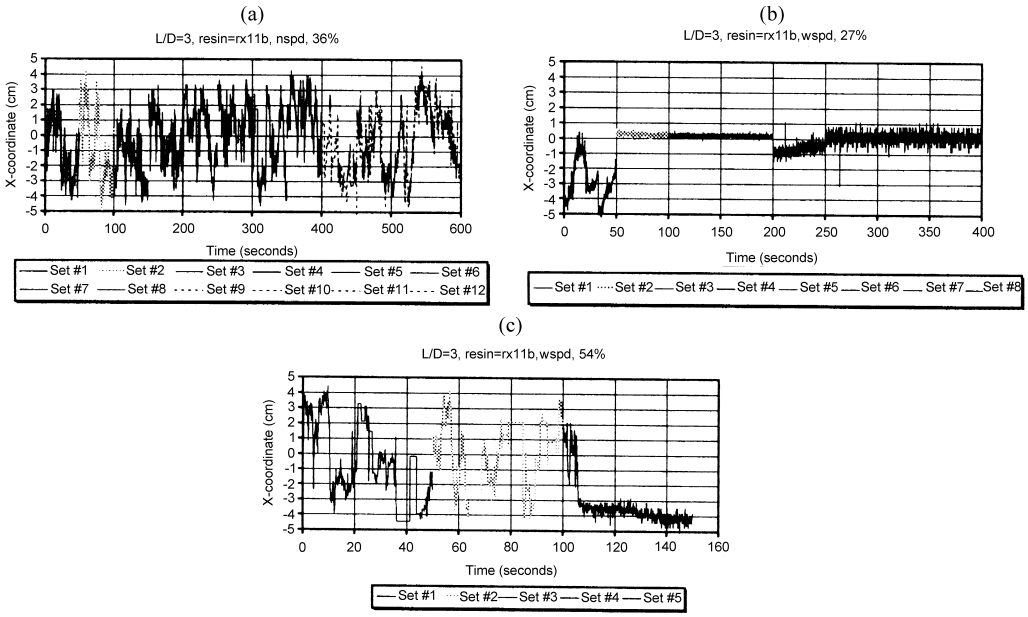

Fig. 10. *X*-position variability for the data of Fig. 9.

are presented. Good Gaussian and Lorentzian behavior is observed for most cases. Small changes in the profiles are observed with changing gas velocity. Although the peaks of the frequency distributions are around zero, the particle horizontal velocities can vary up to more than 25 cm/s and on occasion reach velocities up to 90 cm/s.

Fig. 14 shows the corresponding frequency distribution for the *Z*-positions for WPE and NPE sets of experiments. The first WPE set of experiments shows that the particle spent the duration of the experiment in the top two-thirds of the reactor. The same behaviour was observed for the low rate tests of sample NPE, while the higher rate tests of this sample moved along the whole length of the column. The second set of experiments of sample WPE shows that unless the fluidization numbers are higher than 2.5 the particle movement is highly localized. Unlike the *X*-position plots, there is no clear fit for the *Z*-position data.

Finally, Fig. 15 shows the frequency distributions for the *Z*-velocities of both WPE and NPE sets of experiments. The results are similar to the ones observed with the *X*-velocity. At this point in our research, we have not quantified the significance of such a similarity.

3.4. X-ray Computer Assisted Tomography

Several sets of CAT scanning images were collected at different locations around the proximity of the pressure transducers. Voidage images were calculated and the voxel, slice and column voidage were obtained as a function of operating conditions. The results obtained were similar to the results reported elsewhere [2,3,9,10]. An example is shown in Fig. 16. The main observation from the CAT scanner images is that there were visible high or low voidage regions indicating that the sequence of bubbles and solid flow pathways were identified. In other sets of images (not presented here) the voidage maps were more or less evenly distributed across the bed cross-sections. The combination of CAT scanning and X-ray imaging confirms that by the time the bubbles reach the first pressure transducer, the major pathways for bubble flow have been formed. In addition to the above and contrary to our previous work, we have found that violent motion of solids can give artifact-like accumulation of these solids in certain positions in the bed. This accumulation is currently under further study. Of particular interest in Fig. 16 is the variability of voidage in one cross-section as it can be seen in the

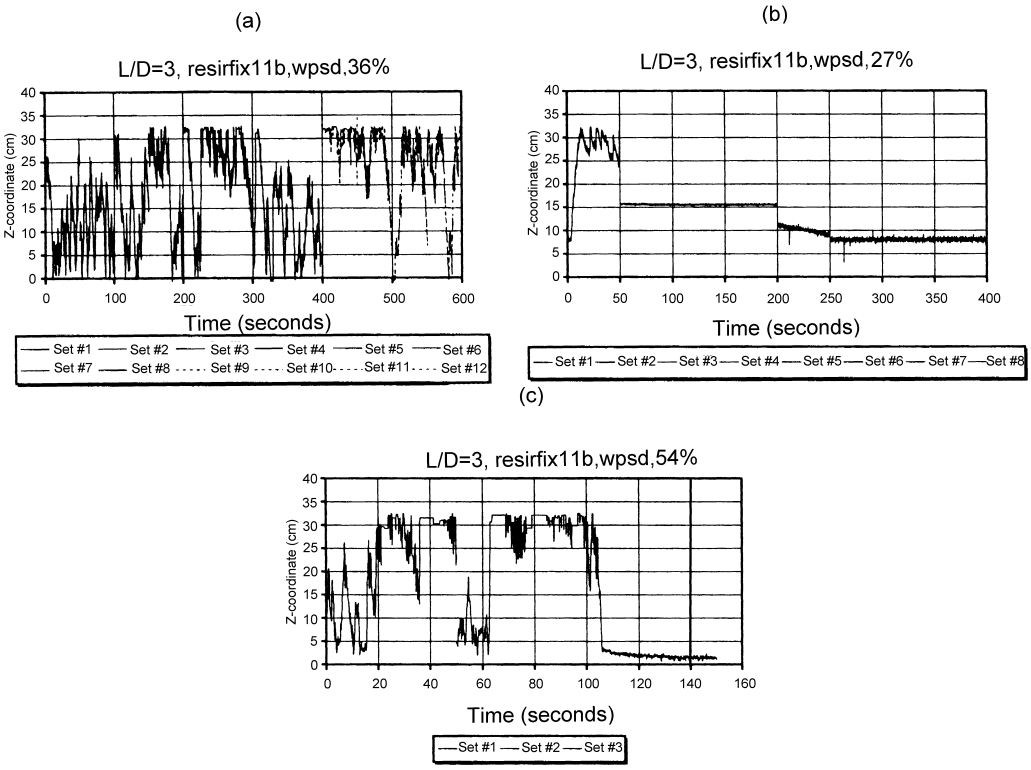

Fig. 11. *Z*-position variability for the data of Fig. 9.

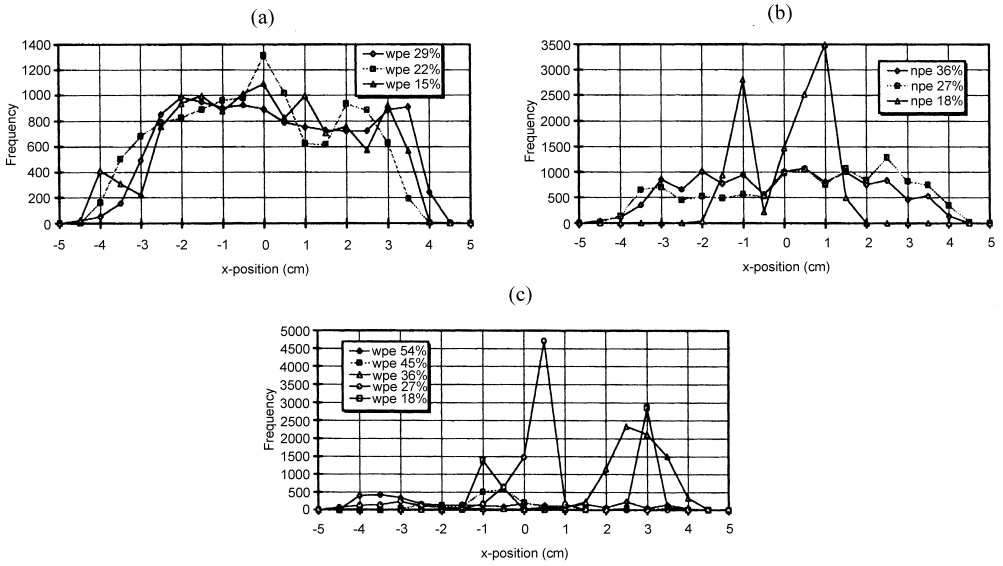

Fig. 12. Frequency distribution for *X*-positions for WPE and NPE sets of experiments.

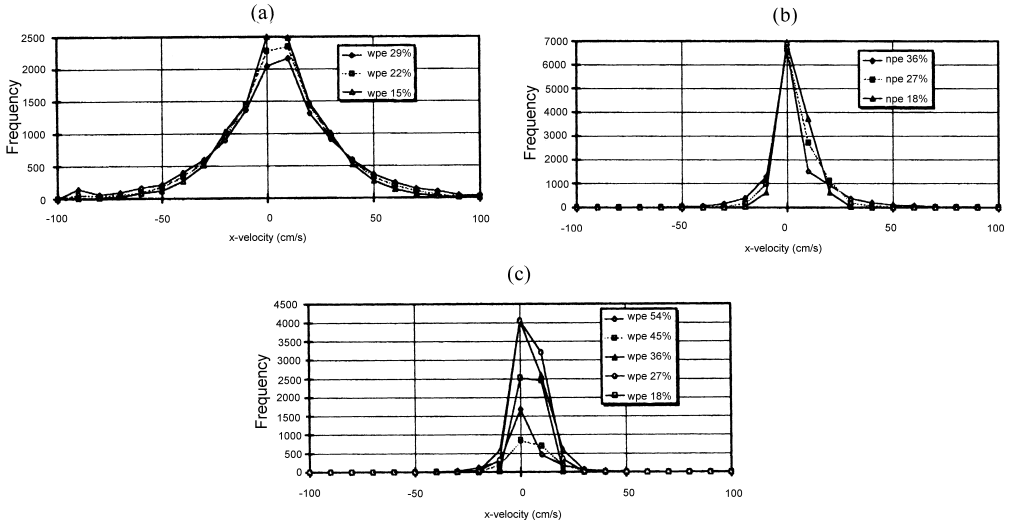

Fig. 13. Frequency distributions for *X*-velocities for WPE and NPE sets of experiments.

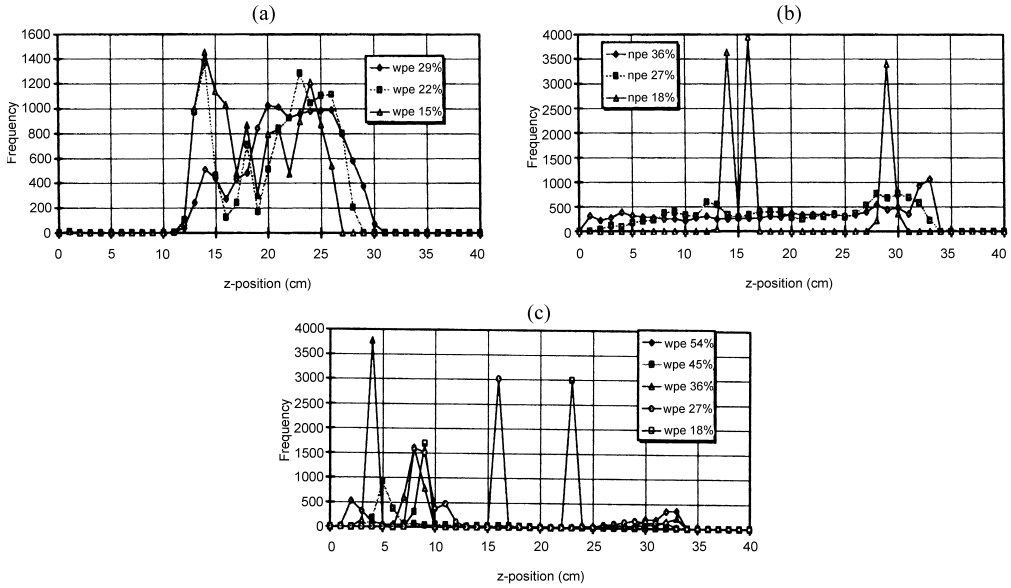

Fig. 14. Frequency distribution for *Z*-positions for WPE and NPE sets of experiments.

figure. Since all images represent the same location in the bed one can see how different the voidage patterns are and establish a field of voidage for use in future modeling. This work is also under further study.

3.5. General observations

In the methodology presented in this paper, all the major flow components of a gas–solid fluidized bed were measured using independent measurement

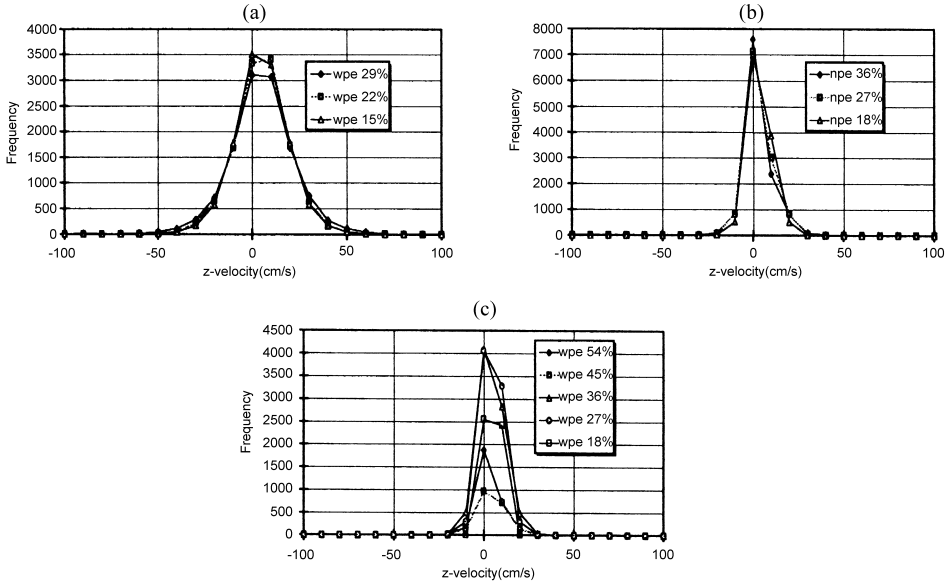

Fig. 15. Frequency distributions for *Z*-velocities for WPE and NPE sets of experiments.

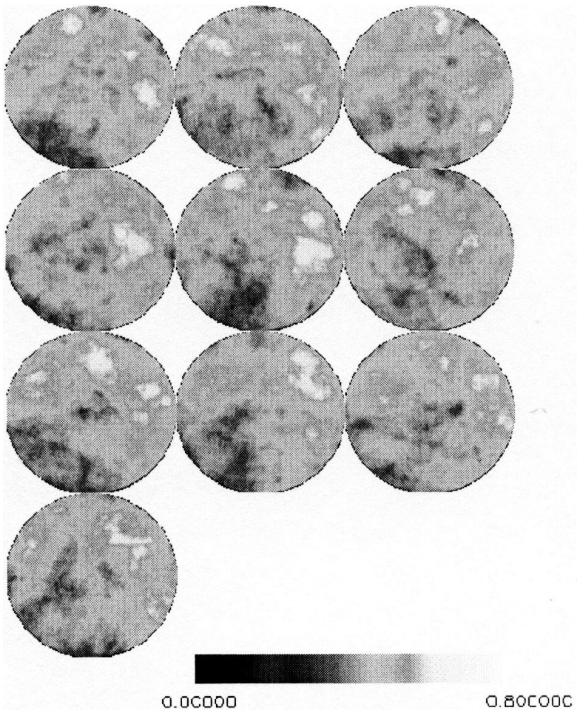

Fig. 16. CAT scanning images of PE resin at gas velocity of 23.2 cm/s and at 7 cm from the distributor plate.

techniques and at the same locations. Bubble location and properties, solid circulation, trajectories and velocities and overall bed voidage were measured as a function of operating conditions. These measurements provide more than an adequate description of the hydrodynamics of the bed and can be used to verify available CFD models. Although the detailed examination of the implications of each measurement will be addressed in separate studies, it is fair to say that tools are available for vigorous testing of available CFD models. Such an approach is currently being followed in our laboratory with commercially available software.

Unfortunately while pressure measurements are capable of giving an indication of overall conditions in the column, or may give information about the flow regime, they cannot give detailed information about the flow as a function of position in the column. For example subtracting the mean pressure at one point in the column from another can give the mean hold up between those two places in the column. However, CT imaging can measure the hold up at many levels between the pressure port and provides the hold up as a function of radial and angular position at each height in the column. Variations in the hold up field can be measured by taking many images at the same height.

These images can then be analyzed to give quick and simple estimates of the fluid flow bypassing the solid through the bubbles for example, or the distribution of bubbles can be measured.

Measurement of the standard deviation of the pressure sampled in a column has been used to determine the changes in flow regime. While this is not commonly done for the transition from bubbling to slugging the transition from bubbling to turbulent or slugging to turbulent has been determined by measuring changes in the standard deviation of the pressure. However it has been demonstrated that this transition is a function of the measurement technique — and in any case it is not a direct measurement of what is happening in the column. It would make more sense to define regime transitions as being where there is a change in the bubble or void characteristics, or where the bubbles/voids reach a certain dimensionless size. It is assumed that such changes will be reflected in the standard deviation of the pressure signal. If possible it makes much more sense to directly measure the void properties which is easily done using fluoroscopy.

A further assumption commonly made is that the frequency of some critical phenomena in the column is reflected in frequency of the pressure signal — however, without a direct measurement of the bed behavior this cannot be verified. Placing a probe in the bed will not only change the nature of the bed by adding internals but will not give a measurement of the bed behavior — only of the local behavior. Fluoroscopy and particle tracking both have the capability to measure the frequency and the velocity of phenomena in the bed.

No one technique is capable of measuring everything that happens in a fluidized bed and the traditional methods do have their place. The single biggest advantage to the systems here is the ability to carry out particle tracking experiments which give measurements of the bed movements — this is almost impossible to carry out with any accuracy using traditional methods. Everything else which the CT imaging and fluoroscopy can measure can also be measured using probes — however, probes can only give a measurement at a point. Even if several probes are used or one used in several places some assumptions about the overall bed behavior are necessary to convert these point measurements to overall measurements. Using the imaging techniques these assumptions are reduced, and can in some cases they can be tested. This gives better overall measurements of the bed behavior.

4. Conclusions

- X-ray imaging, pressure response analysis, radioactive particle tracking and X-ray tomography have been sequentially used to analyze gas–solid fluidized beds with emphasis in air/polyethylene systems.
- Bubble patterns, particle trajectories, stagnant locations in the bed and circulation patterns have been identified.
- For superficial gas velocities up to 40 cm/s, particle velocities of up to 90 cm/s and bubble velocities of up to 140 cm/s were measured.
- The study proved that all the necessary information needed to verify CFD models can be collected in a single laboratory with a simple sequence of experiments.

Acknowledgements

The authors wish to acknowledge financial assistance from NOVA Chemicals, Trojan Technologies and the Natural Sciences and Engineering Research Council of Canada.

References

[1] J.G. Yates, S.J.R. Simons, Int. J. Multiphase Flow 20 (Suppl.) (1994) 297–330.
[2] A. Kantzas, AIChE J. 40 (1994) 1254–1261.
[3] A. Kantzas, I. Wright, N. Kalogerakis, Chem. Eng. Sci. 52 (1997) 2023–2035.
[4] A. Kantzas, N. Kalogerakis, Chem. Eng. Sci. 51 (1996) 1979–1990.
[5] F. Larachi, J. Chauki, AIChE J. 41 (1995) 439–443.
[6] D. Moslemian, N. Devanathan, M. Dudukovic, Rev. Sci. Instrum. 63 (1992) 4361–4372.
[7] J.P.K. Seville, C.J. Broadbent, T.W. Martin, J.D. Parker, T.D. Beydon, in: J.F. Large, C. Larguiere (Eds.), Proc. Fluidization VII, AIChE, Engineering Fundation, 1996.
[8] T. Zarabi, A. Kantzas, Can. J. Chem. Eng. (1999), in press.
[9] J. Song, C.L. Hyndman, R.K. Jakher, K. Hamilton, S. Kryuchkov, A. Kantzas, Chem. Eng. Sci. 54 (1999) 4967–4973.

[10] A. Kantzas, K. Hamilton, T. Zarabi, A. Bhargava, I. Wright, G. Brook, J. Chen, Chem. Eng. J. 77 (2000) 19–25.
[11] F. Li, I. Wright, K. Hamilton, C. Hyndman, A. Kantzas, Presented at the 49th Canadian Chemical Engineering Conference, Saskatoon, Saskacthewan, October 3–6, 1999.
[12] I. Wright, M.E. Thesis, University of Calgary, 1999.
[13] W.K. Kars, S.P. Sutherland, G.L. Osherg, I&E.C. Fundamen. 6 (1967) 499–504.
[14] G.S. Lee, S.D. Kim, J. Chem. Eng. Jpn. 21 (1988) 515–521.
[15] Z. Fan, G.T. Chen, B.C. Chen, H. Yvan, Powder Technol. 62 (1990) 139–145.
[16] O. Winler, AIChE J. 14 (1968) 426–434.
[17] S. Kryuchkov, A. Kantzas, K. Hamilton, Presented at the 49th Canadian Chemical Engineering Conference, Saskatoon, Saskacthewan, October 3–6, 1999.
[18] I.W. Wright, A. Kantzas, K. Hamilton, Presented at the 49th Canadian Chemical Engineering Conference, Saskatoon, Saskacthewan, October 3–6, 1999.